Full paper

In situ visualization of sodium transport and conversion reactions of FeS$_2$ nanotubes made by morphology engineering

Libing Yao[a,1], Weiwei Xia[a,1], Hongtao Zhang[a], Hui Dong[a], Huolin L. Xin[b,*], Peng Gao[c], Ran Cai[a], Chongyang Zhu[a], Yi Wu[a], Meng Nie[a], Shuangying Lei[a], Litao Sun[a,**], Feng Xu[a,***]

[a] *SEU-FEI Nano-Pico Center, Key Laboratory of MEMS of Ministry of Education, Southeast University, Nanjing, 210096, China*
[b] *Department of Physics and Astronomy, University of California, Irvine, CA, 94720, United States*
[c] *Electron Microscopy Laboratory, School of Physics, Peking University, Beijing, 100871, China*

A B S T R A C T

Iron disulfide (FeS$_2$), existing in nature as pyrite, holds great promise as a conversion-type anode material for sodium-ion batteries (SIBs), owing to its low cost and high theoretical capacity. However, the large volume expansion and the sluggish electrode reaction kinetics during conversion reactions impede its large-scale practical application in SIBs. Here, we demonstrate the utilization of morphological engineering to achieve poly-crystalline FeS$_2$ nanotubes (NTs) consisting of tiny FeS$_2$ crystallites. *In situ* transmission electron microscopy observations reveal that 1D shape can afford straight pathways for Na transport to expedite reaction kinetics, and poly-crystalline structure can buffer large volume expansion and structural strain. Furthermore, high-resolution imaging and electron diffraction were utilized to track phase evolution associated with conversion reactions in real time. We have identified an intercalation-conversion reaction mechanism from the FeS$_2$ phase to the Na$_2$S + Fe phases via the intermediate NaFeS$_2$ phase upon initial sodiation. Impressively, a reversible and symmetric conversion reaction between NaFeS$_2$ phase and Na$_2$S + Fe phases is established during subsequent sodiation−desodiation cycles. Notably, this is the first report of FeS$_2$ NTs investigated for secondary battery electrode material. This work not only provides valuable insights into sodium storage mechanism of FeS$_2$ material, but also corroborates the pivotal role of morphology engineering in optimizing the microstructure of electrode materials for advanced SIBs.

1. Introduction

As a mature energy storage technology, rechargeable lithium-ion battery (LIB) has been widely used in consumer electronics and electric vehicles. However, due to the finite lithium resources on Earth, unremitting efforts have been devoted to exploring alternative batteries with viable charge carriers, among which sodium-ion batteries (SIBs) are fascinating because of the abundant sodium reserves [1–3]. As a neighboring alkali metal in the periodic table, sodium shares similar physicochemical properties with lithium. For instance, they both possess one loosely held electron in their valence shell (Li:[He]2s^1, Na:[Ne]3s^1) and comparable standard electrode potential ($\varphi_{Li(+)/Li} = -3.04$ V, $\varphi_{Na(+)/Na} = -2.71$ V), implying that the LIB technology can be presumably transferred to the SIBs [4,5]. However, it must be noted that

Na ions congenitally possess larger ionic radius (Na$^+$: 1.02 Å *vs.* Li$^+$: 0.76 Å) and heavier atomic mass (Na: 22.99 g mol^{-1} *vs.* Li: 6.94 g mol^{-1}), inevitably resulting in large volume expansion, sluggish electrode kinetics, and low energy density in SIBs [6–8]. These shortcomings would be expected to be resolved by hunting for suitable electrode materials and adopting morphology engineering.

Environmentally benign and naturally abundant iron disulfide (FeS$_2$), existing as pyrite in nature, has emerged as an anode material for SIBs featuring high energy density and reversible charge-discharge capability [9,10]. As a conversion-type electrode material, FeS$_2$ can deliver a high theoretical capacity of 894 mAh g^{-1}, based on the storage of four Na$^+$ per FeS$_2$ forming Na$_2$S and Fe with a full sodiation [11,12]. Although the currently developed FeS$_2$ anodes in SIBs can offer an enhanced cycle life of 20,000 cycles at 1 A g^{-1}, their capacities (at

most 200 mAh g^{-1}) are far below the above theoretical value [13]. This awkward situation is attributed to the large volume expansion of up to ~280% (based on the conversion from the initial FeS$_2$ to the final Na$_2$S and Fe phases) and the low electronic conductivity and poor ionic diffusivity of FeS$_2$ particle-based electrode [11,14,15]. As a result, the structural pulverization and high internal resistance occur in FeS$_2$ electrode, thereby resulting in sluggish electrode reaction kinetics and substantial capacity fading especially at high current rates [12,16]. To circumvent the undesired volume expansion, recent works employ the limited potential windows to ensure the sodium storage process only with the intercalation reaction [13,17]. However, this strategy not only sacrifices the battery energy density, but also impedes in-depth understanding of the full sodiation mechanism [11,18].

In this work, we have elaborately designed one-dimensional (1D) tube-like FeS$_2$ nanostructures consisting of numerous tiny FeS$_2$ crystallites. This morphology engineering, which endows this material with 1D hollow form and poly-crystalline structure, is expected to not only provide straight ionic transport pathway to improve ionic diffusion kinetics, but also withstand large volume expansion and structural strain from the conversion reaction. To corroborate these merits of such FeS$_2$ NTs, we use *in situ* transmission electron microscopy (TEM) technique to track ionic transport and structural evolution in real time during the sodiation-desodiation cycles. We identify an intercalation-conversion reaction mechanism upon the first full sodiation, in which intermediate phase NaFeS$_2$ appear and then is converted to Fe phase dispersed in Na$_2$S matrix. However, the first desodiated products is found to be the NaFeS$_2$ phase, rather than the initial FeS$_2$ phase. During subsequent cycles, a reversible and symmetric phase transformation between NaFeS$_2$ phase and Fe + Na$_2$S phases is established. Although the 1D hollow NTs undergo multiple volume expansion and contraction, no pulverization and cracking are observed. To the best of our knowledge, this is the first report of hollow FeS$_2$ NTs investigated for secondary battery. Our work not only introduces morphology engineering strategy to achieve ideal ionic transport kinetics in FeS$_2$ NTs, but also provides a comprehensive and detailed understanding of the electrochemical sodiation process and mechanism of this material.

2. Experimental section

2.1. Preparation of FeS$_2$ NTs

All the regents are of analytical purity and were used without further treatment. In a typical procedure, 1 mmol Fe(NO$_3$)$_3$·9H$_2$O and 4 mmol NH$_2$CSNH$_2$ were dissolved in 50 mL ethylenediamine and stirred for 1 h to form a uniform solution, which was transferred into a Teflon-lined stainless autoclave, sealed and maintained at 200 °C for 45 h. After cooling to room temperature, the black products were washed with deionized water and ethanol for several times, followed by drying in vacuum at 60 °C for overnight. The final FeS$_2$ NTs were obtained by annealing at 300 °C in Ar for 2 h.

2.2. In situ electrochemical experiments

The *in situ* nanobattery observations were conducted in transmission electron microscopy (TEM, FEI Tecnai 200 kV & Titan 300 kV) with Nanofactory TEM-STM holder. High-resolution TEM images with a fast responding charge-coupled device (CCD) camera were carried out for *in situ* observing the electrochemical behaviors of FeS$_2$ NTs with the assistance of selected area electron diffraction (ED). The FeS$_2$ NTs attached to an Au rod by conductive sliver colloid to ensure a good electrical, were used as working electrode. Bulk Na metal which was scratched by a shaped W tip worked as the counter electrode; a natural oxidized layer of NaO$_x$, allowing the transport of sodium ions, was regarded as solid electrolyte. The counter electrode can contact the working electrode by manipulating the piezo-driven stage with nanometer precision. Once a contact was made, the negative or positive

potentials were applied, thereby initiating the electrochemical sodiation/desodiation process. Scanning electron microscopy (SEM) images were obtained on a microscope (Ultra Plus, Zeiss) operated at 15 kV to study the morphology of the samples.

2.3. Electrochemical measurements

The electrochemical performance of the prepared materials was investigated by CR2025 half-cells. The working electrodes were prepared by mixing the active material, acetylene black, and poly-vinylidene fluoride (PVDF) with a weight ratio of 70:20:10 in 1-methyl-2-pyrrolidinone (NMP) with string for 12 h. Then, the metallic sodium foils were used as both the reference and counter electrodes. Whatman glass microfiber filter membrane as the separator, and the solution of 1 M NaClO$_4$ in ethylene carbonate (EC)/dimethyl carbonate (DMC) (1:1 vol% with 5 vol% fluoroethylene carbonate (FEC)) as the electrolyte. The discharge-charge performance of cells was measured at a current density of 0.2 C (1 C = 894 mAh g^{-1}) in the potential range of 0.01–3.0 V on LANHE battery test system. FeS$_2$ powders were purchase from Alfa Aesar company without further purify.

3. Results and discussion

The detailed formation process of FeS$_2$ NTs is illustrated in Fig. 1a and the preparation details are delineated in Experimental Section. The formation mechanism of hollow FeS$_2$ NTs is attributed to the Kirkendall effect, as indicated by the inset of the time-sequence morphology evolutions in Fig. 1a. High-temperature treatment was used for further improve the sample crystallinity. SEM image in Fig. 1b shows the FeS$_2$ NTs are several micrometers in length. The enlarged SEM images are further supplied in Fig. S1 to illustrate that the as-synthesized FeS$_2$ samples have the hollow structure. Fig. 1c presents a low-magnification TEM image of FeS$_2$ NTs with diameters ranging from 100 to 250 nm. The magnified TEM image of individual FeS$_2$ NT was illustrated in Fig. 1d, which reveals FeS$_2$ NT is composed of tiny nanoparticles with a grain size of ~10 nm. The inset of Fig. 1d shows that the abundant sub-nanometer gaps exist among the FeS$_2$ nanoparticles. The nanoparticles are identified as pyrite FeS$_2$ by high-resolution TEM (HRTEM) in Fig. 1e, in which the interplanar spacing of 0.27 nm matches with the (200) plane of pyrite FeS$_2$ (JCPDS No.42–1340) [13,19]. Furthermore, the electron diffraction (ED) pattern corresponding to Fig. 1d is shown in Fig. 1f, which can be well indexed to different polycrystalline diffraction rings with (111), (200), (211), (220), (311) and (222) planes of pyrite FeS$_2$ [20]. Fig. 1g illustrates the atomic structure model of the pyrite FeS$_2$, in which Fe^{2+} forms a face-centered cubic lattice with each Fe octahedrally coordinated by disulfide bonds of the form S$_2^{2-}$. The high angle annular dark field (HAADF) image and EDS mappings are further presented in Fig. 1h–j. The HAADF image show a clear one-dimensional and hollow structure. The corresponding EDS mappings show the uniform distribution of Fe and S elements (Fig. 1i and j).

The *in situ* electrochemical experimental setup for FeS$_2$ NTs anode in SIB is schematically illustrated in Fig. 2a. Once the NaO$_x$/Na electrode was in contact with the NTs, the electrochemical sodiation process was initiated by applying a constant bias of −2.0 V with respect to the NaO$_x$/Na electrode [21–23]. Fig. 2b and c shows the panoramic TEM images of a single FeS$_2$ NT before and after sodiation, respectively. Obviously, the contrast variation in radial size characterized by an expansion from 187 nm to 215 nm was observed after full sodiation. According to the referenced position (marked by blue arrow in Fig. 2c), the longitudinal elongation along the NT was from 472 nm to 541 nm. The whole morphology evolution process of sodiation was recorded as a series of still TEM images, as shown in Fig. 2d–h (see also Movie S1 in Supporting Information). From that we can see that the sodiation reaction front (SRF, marked with red arrows) occurred at the end of the contact with NaO$_x$/Na electrode, and gradually propagated toward the other end. No cracking or fracturing of FeS$_2$ NT was ever observed even
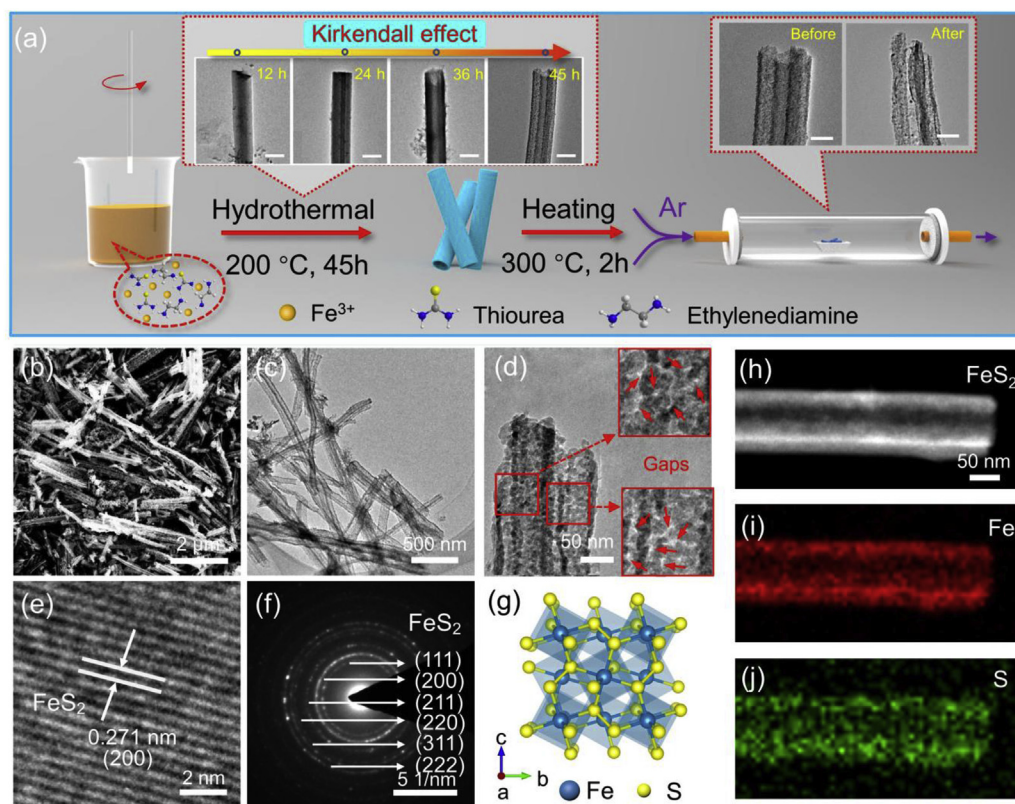
Fig. 1. (a) Schematic illustration of the sample synthesis configurations. (b) SEM image of the FeS_2 NTs. (c) TEM image reveals the tube-like shape of FeS_2. (d) The magnified TEM image of FeS_2 NTs, suggesting that each NT is composed of tiny FeS_2 nanoparticles with size of ~10 nm. The inset shows that the abundant sub-nanometer gaps exist among the FeS_2 nanoparticles. (e) The HRTEM image of FeS_2 NT with a typical lattice distance of 0.27 nm. (f) The ED patterns show the polycrystalline feature of FeS_2 NTs. (g) Crystal structure model of the cubic spinel FeS_2. (h–j) The HAADF image of a pristine FeS_2 NT and corresponding element mappings.
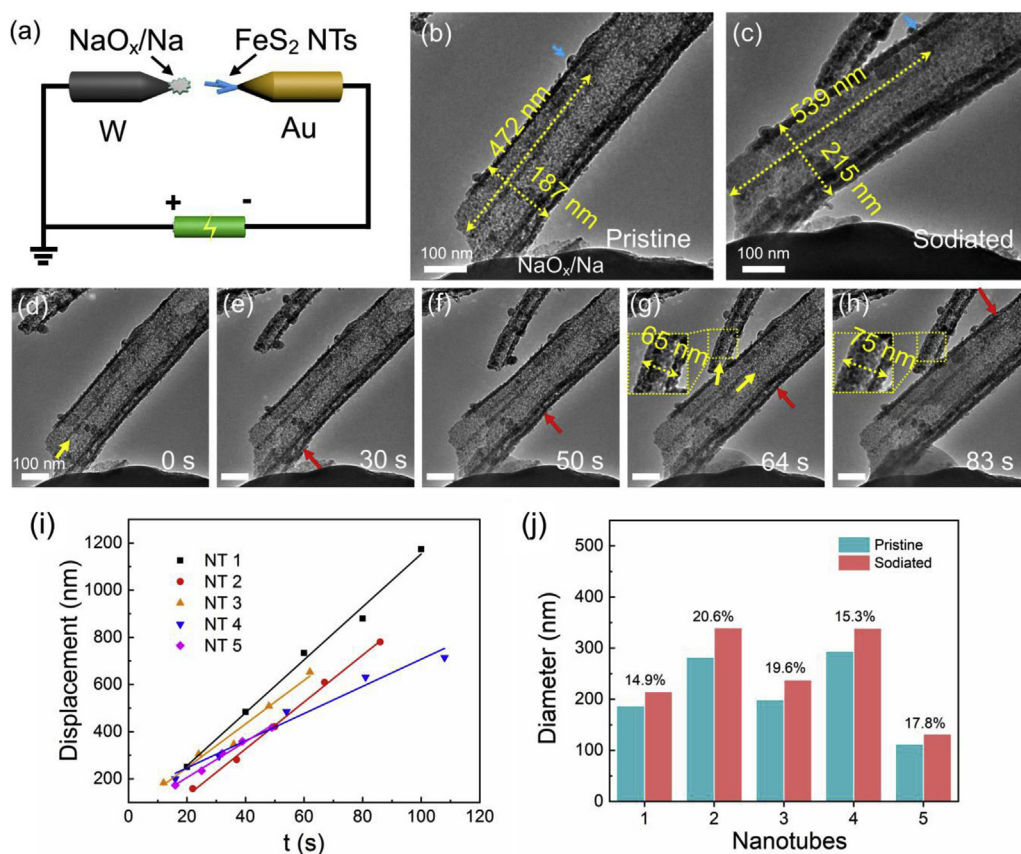

Fig. 2. (a) Schematic illustration of the experimental setup for *in situ* electrochemical sodiation/desodiation. TEM images in (b) and (c) show the pristine and fully sodiated morpholoties of a FeS_2 NT, respectively. (d–h) The morphology evolution of the FeS_2 NT during the first sodiation process. (i) Relationship between sodiation position and sodiation time recorded from five FeS_2 NTs, showing homogeneous sodiation behaviors along the FeS_2 NTs. (j) The histogram shows the diameter variation of the five FeS_2 NTs before and after sodiation.

after full sodiation, in spite of obvious radial expansion and axial elongation. This structural endurance is better than most of conversion-typed materials, and the reasons for structural stability can be explained as the following two possible factors [24–26]. First, the hollow NTs can offer sufficient inward space to tolerate the radial expansion; second, the polycrystalline framework of NTs characterized by numerous gaps among the FeS$_2$ nanoparticles can effectively buffer the stress, which mainly induced by the volume expansion and conversion reactions. Furthermore, we also observed a nonnegligible sodiation phenomenon for the lateral transport of Na$^+$ between the contacting NTs. As shown in the inset in Fig. 2g,h, a pristine NT can be sodiated by a fully sodiated FeS$_2$ NT, which started from their contacted position, and finally showed a radial expansion of around 15% (from 65 to 75 nm). The lateral sodiation behavior between the adjacent NTs indicates a small interfacial sodiation barrier between the as-synthesized NTs [27].

Supplementary data related to this article can be found at https://doi.org/10.1016/j.nanoen.2019.03.080.

To probe transport dynamics of sodium ions in hollow NTs, the SRF displacements (*d*) of five different FeS$_2$ NTs as a function of time (*t*) are plotted in Fig. 2i. All the curves exhibit linear correlation, suggesting that the SRF motion speed in each NT is uniform. The motion speed is calculated to be ~ 6–11 nm s^{-1}, indicating a low diffusion barrier in the polycrystalline NTs [28]. We believe that the low diffusion barrier can be attributed to the existence of numerous gaps among FeS$_2$ nanoparticles. The size of the gaps is large enough to allow the diffusion of Na$^+$ ions (ionic radius: 1.02 Å) via the gaps [29–31]. Different SRF motion speeds for varying NTs should be associated with sample size, contact condition, and local sodium ions concentration [32]. In Fig. 2j, we find that the radial expansion rates of the five fully sodiated FeS$_2$ NTs are similar (~ 15–20%). They exhibit no apparent differences in morphology, and no cracking or fracturing are found.

To better understand the structural stability of the FeS$_2$ NTs, the schematic illustration of nonuniform stress distribution during the sodiation process is shown in Fig. 3. As sodium ions concentration increased, the Young's modulus of a FeS$_2$ NT would inevitably change, which would lead to the uneven stress distribution in a FeS$_2$ NT. During the initial stage of the intercalation reaction, the stress change is small. The following conversion reaction is the main reason for the large volume expansion, accompanying with large stress changes on SRF, as shown in Fig. 3a. From the top view along the axis of a sodiating NT, the sufficient internal space provides an effective buffer for stress variation (Fig. 3b). This is consistent with the *in situ* observation that the FeS$_2$ NT has a moderate volume expansion during the sodiation process. Therefore, the as-prepared polycrystalline FeS$_2$ NTs featuring plenty of micro-gaps between tiny nanoparticles ensures the structural stability during repeated sodiation/desodiation cycles.

As shown in Fig. 4a–c, a single NT shows obviously swelled upon an initial sodiation. The NT was then coated with a crystalline layer after full sodiation (Fig. 4c) with a radial expansion rate of 20% (from 190 nm to 228 nm). Fig. 4d is a magnified TEM image corresponding to
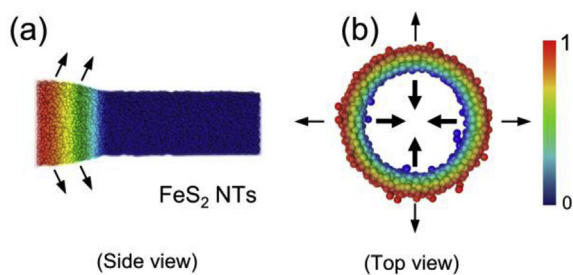
the region marked by the red box in Fig. 4c. We can clearly see that the fully sodiated NT is featured by numerous nanograins and coated with a thin layer of ~ 9 nm. Further, we employed the ED to track the structural and phase evolutions upon sodiation process. The layer was identified as Na$_2$S phase according to the diffraction rings of (220), (311), (331), and (422) planes in Fig. 4g. The ordered lattice fringes of 0.384 nm in Fig. 4h are in accordance with the (111) plane of Na$_2$S phase [33–35].

The ED patterns in Fig. 4e − g show phase transformations upon initial sodiation process. Diffraction rings of FeS$_2$ disappeared gradually, and the distinct diffraction rings attributed to NaFeS$_2$ (JCPDS No. 34–0935) appeared [17,36], as shown in Fig. 4f. The detailed analysis process for NaFeS$_2$ phase can also found in Fig. S2 (Supporting Information). Fig. S5 (Supporting Information) presents the crystal structures of NaFeS$_2$ phase along [010] and [001] directions, clearly showing a layer structure. The number of Na ions in NaFeS$_2$ differs from that of Li ions in Li$_{1.13}$FeS$_2$ phase as reported by Chen et al. in Li–FeS system [37], which may be related to the difference in the ionic radius between Na and Li ions. The intermediate products of NaFeS$_2$ were subsequently transformed to metallic Fe and Na$_2$S phases after full sodiation, as corroborated by the ED pattern in Fig. 4g. Fig. 4h shows HRTEM image of the fully sodiated NT, and the lattice spacings of 0.20 nm and 0.38 nm correspond to the (110) plane of cubic phase Fe (JCPDS No. 06–0690) [3,38,39] and the (111) plane of cubic phase Na$_2$S (JCPDS No. 47–1698) [33,34], respectively. Likewise, the detailed analysis process of the Na$_2$S and Fe phase is also presented in Fig. S3 (Supporting Information). Moreover, the morphology evolution of other FeS$_2$ NTs during the sodiation process is supplemented in Fig. S4 (Supporting Information), which obviously exhibits the characteristics of the conversion reaction. Consequently, a two-step conversion reaction mechanism during the first sodiation of FeS$_2$ NTs is revealed as follows: FeS$_2$ + Na$^+$ + e$^-$ → NaFeS$_2$ and NaFeS$_2$ + 3Na$^+$ + 3e$^-$ → 2Na$_2$S + Fe. We further tracked the time-resolved motion of SRF interface where the conversion reactions occurred, as shown in Fig. 4i–k (see also Movie S2 in Supporting Information). The NT is divided into two distinct interior contrasts by a moving SRF interface occurring from the lower left corner, as indicated by white dashed line. The diffusivity is estimated to be $\sim 3.1 \times 10^{-3}$ nm^2 s^{-1} on the basis of increasing conversion area over time. However, it is worthwhile to note that this calculation only gives us an approximate value of the diffusivity, because some uncertain factors can possibly influence the estimation. As the SRF interface propagated along the NT, the original FeS$_2$ nanoparticles were converted into numerous tiny Fe nanograins coincident with expansion of the NT. Fig. S6 (Supporting Information) shows the HAADF image and the corresponding elemental mappings of the sodiated FeS$_2$ NT, which indicates the uniform distribution of Fe, S, and Na elements.

Supplementary data related to this article can be found at https://doi.org/10.1016/j.nanoen.2019.03.080.

The reversible intercalation and deintercalation of sodium ions in electrode materials is fundamental for rechargeable SIBs [32]. To initiate the desodiation process, a reversed constant bias was applied to extract sodium ions from the sodiated FeS$_2$ NT, as shown in Fig. 5a and b and Movie S3. With the going of sodium ions extraction, a slight diameter shrinks of about 9.5% (from 189 to 171 nm) was observed within 33 s. ED patterns of the NT were also recorded to identify phase evolution, as displayed in Fig. 5c and d. Upon desodiation, ED patterns attributed to Na$_2$S and Fe phase gradually disappeared. The final diffraction rings were identified as the crystalline NaFeS$_2$ phase (JCPDS No. 34–0935), indicating that the desodiation process was an asymmetric reaction relative to the first sodiation. The reversible phase transformation between the NaFeS$_2$ phase and Fe + Na$_2$S phase can be attributed to the high electrocatalysis active of Fe nanograins, which is related to the crystal size and quantum size effects [40,41]. The Na$_2$S detected by the ED in Fig. 5b could be attributed to the generated Na$_2$S layer during first sodiation process, which was difficult to be

Fig. 3. Schematic illustration showing the nonuniform stress distribution of the tube-like FeS$_2$ upon sodiation process, (a) Side view and (b) Top view along the axis of a NT.
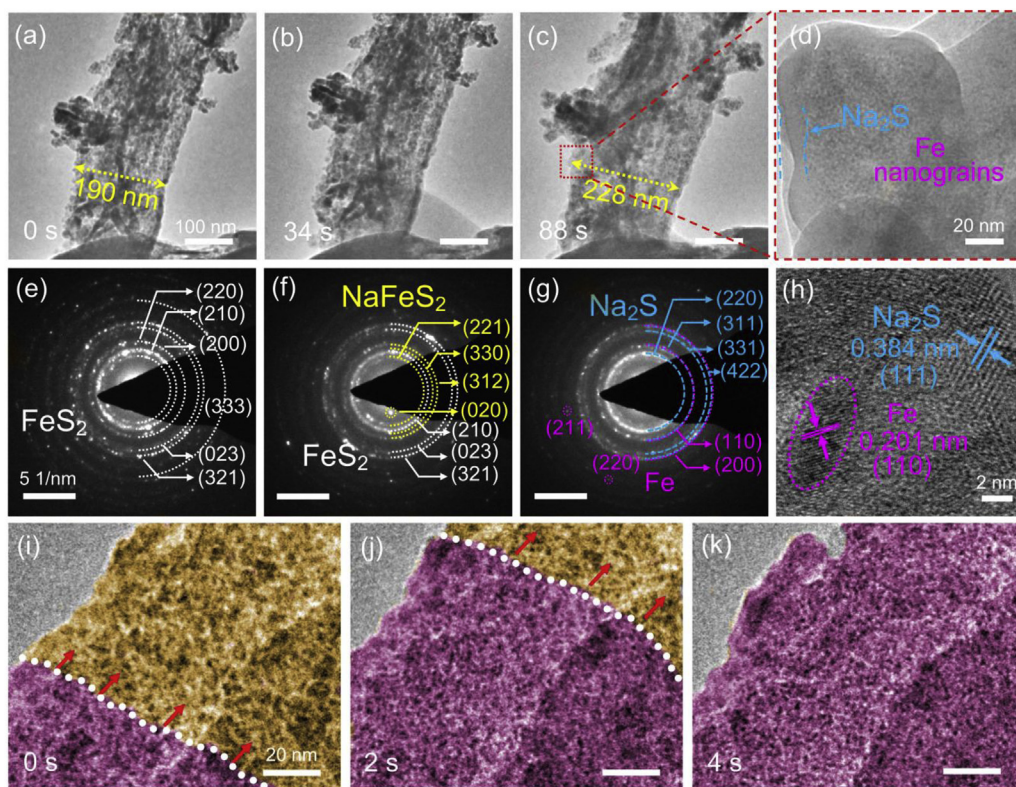
Fig. 4. (a–c) Snapshots of the sodiation process from video, showing the structural evolution of a segment of a FeS$_2$ NT during the first sodiation process. (d) The magnified TEM image of fully sodiated FeS$_2$ NT corresponds to the marked regions in (c). (e–g) The ED patterns correspond to the different sodiation stages of the FeS$_2$ NT in (a–c), revealing a two-step phase transformation process during the first sodiation process. (h) HRTEM image of the fully sodiated FeS$_2$ NT. (i–k) Snapshots of the moving reaction front from video, showing the formation of Fe nanograins embedded in the Na$_2$S matrix.

completely converted upon the subsequent desodiation process. This phenomenon is similar to other metal and carbon electrodes with high surface area and small particle size [42,43]. Overall, the conversion reaction during the first desodiation process can be expressed as follow:

$$2Na_2S + Fe \rightarrow NaFeS_2 + 3Na^+ + 3e^-.$$

Supplementary data related to this article can be found at https://doi.org/10.1016/j.nanoen.2019.03.080.

The HRTEM images were employed to further track local phase evolution during the first desodiation process, as shown in Fig. 5e–i (see also Movie S4 in Supporting Information). Prior to the desodiation in
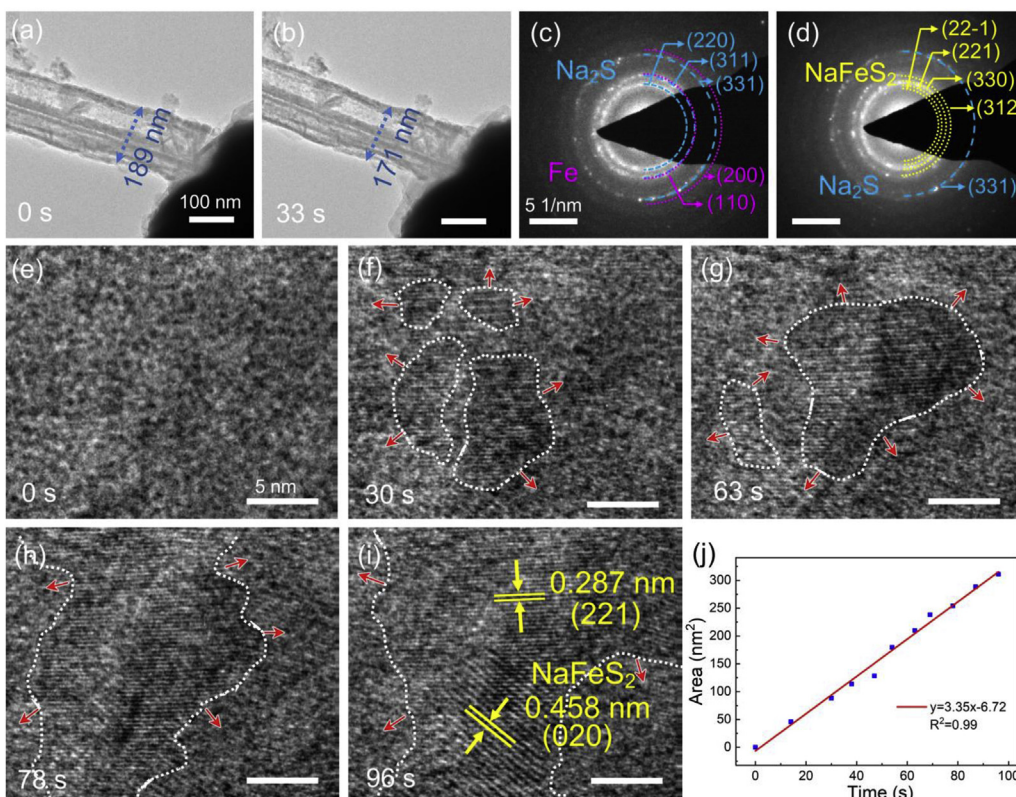

Fig. 5. (a,b) Snapshots of the desodiation process from video, showing the morphological evolution of a sodiated NT before and after the first desodiation. (c,d) The ED patterns correspond to (a,b), revealing that the Fe and Na$_2$S phases are converted into the NaFeS$_2$ phase, rather than the original FeS$_2$. (e–i) High-resolution TEM tracking of the local structural evolution during desodiation of (e) a fully sodiated NT. (f–h) The outlines highlight the striped domains that nucleat quickly and heterogeneously. (i) After ~96 s, individual striped domains merged into a larger one belonging to the NaFeS$_2$ phase. (j) The area of striped domains is plotted as a function of the desodiation time, showing a linear increase with time.
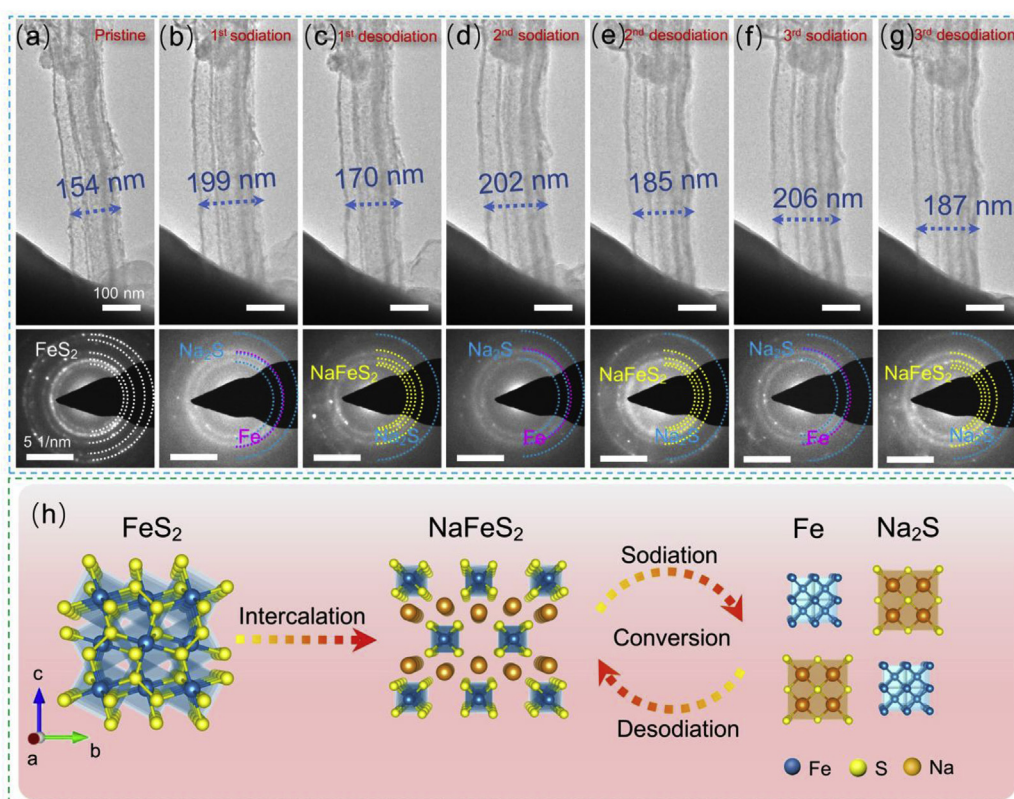
Fig. 6. (a–g) TEM images and corresponding ED patterns show morphological and structural evolutions during the first three cycles of sodiation/desodiation processes of a FeS$_2$ NT. The corresponding ED patterns are shown below. (h) Schematic illustration of the intercalation-conversion mechanism of the FeS$_2$ material during repeated electrochemical charge-discharge cycles.

Fig. 5e, no obvious lattice planes are visible. Once the desodiation was initiated, sodium ions were extracted from the sodiated NT. The observations of multiple oriented domains with clear lattice fringes indicate the emergence of newly formed crystalline areas, which can be indexed as NaFeS$_2$ phase, as highlighted by white dashed lines in Fig. 5f–i. With further extraction of sodium ions, the striped domains gradually expand over time and then merged together. In Fig. 5i, the clear interplanar distances of 0.458 nm and 0.287 nm correspond to the (020) and (221) planes of NaFeS$_2$ phase, respectively [17]. The total area of striped domains within field of vision (nm^2) is plotted as a function of time (s) in Fig. 5j. Evidently, the area of striped domains exhibits a linear increase with time.

Supplementary data related to this article can be found at https://doi.org/10.1016/j.nanoen.2019.03.080.

The structural stability of electrode materials after repeated cycles can ensure long-term and reliable operation of the battery. Therefore, the multicycle electrochemical reactions associated with insertion and extraction of sodium ions in FeS$_2$ NT were carefully evaluated in Fig. 6a–g. (Movie S5, in Supporting Information). Fig. 6a shows a pristine FeS$_2$ NT with a diameter of 154 nm. As shown in Fig. 6b–g, the NT underwent repeated volume expansion and contraction accompanying with multiple structural transformations (as proved by ED patterns). It is gratifying that no cracking or fracturing was formed. The superior structural endurance is as a result of the morphology engineering that enables the 1D polycrystalline FeS$_2$ NTs. Such a morphology can provide more inward expansion space along the radial direction of the NT and abundant inter-nanoparticles micro-gaps within the NT, effectively buffering and releasing the strain induced by the large volume expansion and the violent conversion reactions. On the basis of the above analysis, the reaction mechanism of FeS$_2$ during sodiation–desodiation processes is schematically illustrated in Fig. 6h.

Supplementary data related to this article can be found at https://doi.org/10.1016/j.nanoen.2019.03.080.

Further, the FeS$_2$ NT electrodes were tested at 0.2 C (1 C = 894 mAh g^{-1}) to characterize their cycling ability. The specific capacity of FeS$_2$
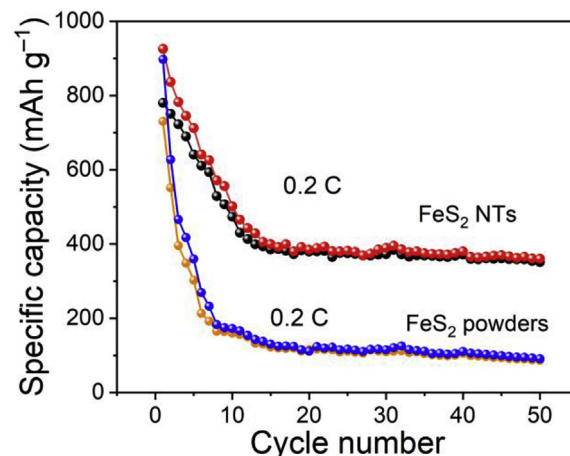

Fig. 7. Reversible charge/discharge capacities of FeS$_2$ NTs and FeS$_2$ powders at a current density of 0.2 C (1 C = 894 mAh g^{-1}).

NTs electrode is maintained at 360.3 mAh g^{-1} after 50 cycles, which is evidently better than 91.2 mAh g^{-1} of the commercial FeS$_2$ powder after 50 cycles, as shown in Fig. 7. Moreover, Fig. S7 (Supporting Information) further presents the TEM images of FeS$_2$ NTs electrode after 6 sodiation–desodiation cycles in the *in situ* experiment and a FeS$_2$ NTs after 50 cycles in a real battery, respectively. No cracks are observed for both samples from the *in situ* experiment and a real battery. Therefore, it is reasonable to believe that tube-like structure has good stability in the sodiation–desodiation cycles.

4. Conclusion

In conclusion, the hollow FeS$_2$ NTs consisting of tiny FeS$_2$ crystallites were successfully synthesized, and the real-time electrochemical sodiation/desodiation behaviors of the FeS$_2$ NTs were for the first time

studied by *in situ* TEM technique with high spatial and temporal resolution. We identify an intercalation-conversion reaction mechanism upon initial sodiation of a FeS_2 NT, in which the intermediate phase $NaFeS_2$ occurs and then converts into the Fe and Na_2S phases as the sodiated products. Upon subsequent desodiation, the Fe and Na_2S phases are transformed into the $NaFeS_2$ phase, rather than the original FeS_2 phase. Such a phase transformation between the $NaFeS_2$ phase and Fe and Na_2S phases is reversible during subsequent cycles. Furthermore, the *in situ* TEM investigation corroborates the pivotal role of morphology engineering in optimizing the microstructure of electrode materials for advanced SIBs. The as-prepared FeS_2 NTs can improve Na ions diffusion kinetics and possess the advantages of accommodating large volume expansion and structural strain. These findings not only help to deepen the understanding of sodium storage mechanism of FeS_2 material, but also pave the way for its large-scale application by providing a facile synthetic strategy of morphology engineering.

Acknowledgements

Appendix A. Supplementary data

Supplementary data to this article can be found online at https://doi.org/10.1016/j.nanoen.2019.03.080.

References

[1] M.D. Slater, D. Kim, E. Lee, C.S. Johnson, Adv. Funct. Mater. 23 (2013) 947–958.
[2] N. Yabuuchi, K. Kubota, M. Dahbi, S. Komaba, Chem. Rev. 114 (2014) 11636–11682.
[3] Y. Chen, X. Hu, B. Evanko, X. Sun, X. Li, T. Hou, S. Cai, C. Zheng, W. Hu, G.D. Stucky, Nanomater. Energy 46 (2018) 117–127.
[4] K. Chayambuka, G. Mulder, D.L. Danilov, P.H.L. Notten, Adv. Energy. Mater. 8 (2018) 1800079.
[5] S. Chen, C. Wu, L. Shen, C. Zhu, Y. Huang, K. Xi, J. Maier, Y. Yu, Adv. Mater. 29 (2017) 1700431.
[6] N. Ortiz-Vitoriano, N.E. Drewett, E. Gonzalo, T. Rojo, Energy Environ. Sci. 10 (2017) 1051–1074.
[7] J.Y. Hwang, S.T. Myung, Y.K. Sun, Chem. Soc. Rev. 46 (2017) 3529–3614.
[8] W. Ren, Z. Zhu, Q. An, L. Mai, Small 13 (2017) 1604181.
[9] Y. Zhu, L. Suo, T. Gao, X. Fan, F. Han, C. Wang, Electrochem. Commun. 54 (2015) 18–22.
[10] W. Zhao, C. Guo, C.M. Li, J. Mater. Chem. A 5 (2017) 19195–19202.
[11] Z. Liu, T. Lu, T. Song, X.Y. Yu, X.W. Lou, U. Paik, Energy Environ. Sci. 10 (2017) 1576–1580.
[12] M. Walter, T. Zuend, M.V. Kovalenko, Nanoscale 7 (2015) 9158–9163.
[13] Z. Hu, Z. Zhu, F. Cheng, K. Zhang, J. Wang, C. Chen, J. Chen, Energy Environ. Sci. 8 (2015) 1309–1316.
[14] K. Chen, W. Zhang, L. Xue, W. Chen, X. Xiang, M. Wan, Y. Huang, ACS Appl. Mater. Interfaces 9 (2017) 1536–1541.
[15] J. Lu, F. Lian, L. Guan, Y. Zhang, F. Ding, J. Mater. Chem. A 7 (2019) 991–997.
[16] X. Xu, J. Liu, Z. Liu, J. Shen, R. Hu, J.W. Liu, L. Ouyang, L. Zhang, M. Zhu, ACS Nano 11 (2017) 9033–9040.
[17] W. Chen, S. Qi, L. Guan, C. Liu, S. Cui, C. Shen, L. Mi, J. Mater. Chem. A 5 (2017) 5332–5341.
[18] Q. Wang, C. Guo, Y. Zhu, J. He, H. Wang, Nano-Micro Lett. 10 (2017) 30.
[19] Z. Hu, K. Zhang, Z. Zhu, Z. Tao, J. Chen, J. Mater. Chem. A 3 (2015) 12898–12904.
[20] G.X. Pan, F. Cao, X.H. Xia, Y.J. Zhang, J. Power Sources 332 (2016) 383–388.
[21] S. Tan, Y. Jiang, Q. Wei, Q. Huang, Y. Dai, F. Xiong, Q. Li, Q. An, X. Xu, Z. Zhu, X. Bai, L. Mai, Adv. Mater. 30 (2018) 1707122.
[22] Q. Liu, T. Yang, C. Du, Y. Tang, Y. Sun, P. Jia, J. Chen, H. Ye, T. Shen, Q. Peng, L. Zhang, J. Huang, Nano Lett. 18 (2018) 3723–3730.
[23] P. Gao, L. Wang, Y. Zhang, Y. Huang, K. Liu, ACS Nano 9 (2015) 11296–11301.
[24] Y. Xiao, S.H. Lee, Y.K. Sun, Adv. Energy. Mater. 7 (2017) 1601329.
[25] Y. Jiang, M. Hu, D. Zhang, T. Yuan, W. Sun, B. Xu, M. Yan, Nanomater. Energy 5 (2014) 60–66.
[26] S. Hariharan, K. Saravanan, P. Balaya, Electrochem. Commun. 31 (2013) 5–9.
[27] F. Xu, L.J. Wu, Q.P. Meng, M. Kaltak, J.P. Huang, J.L. Durham, M. Fernandez-Serra, L.T. Sun, A.C. Marschilok, E.S. Takeuchi, K.J. Takeuchi, M.S. Hybertsen, Y.M. Zhu, Nat. Commun. 8 (2017) 15400.
[28] C. Zhu, F. Xu, H. Min, Y. Huang, W. Xia, Y. Wang, Q. Xu, P. Gao, L. Sun, Adv. Funct. Mater. 27 (2017) 1606163.
[29] Y. Yuan, X. Xia, J. Wu, X. Huang, Y. Pei, J. Yang, S. Guo, Electrochem. Commun. 13 (2011) 1123–1126.
[30] P. Heitjans, S. Indris, J. Phys-Condens. Mat. 15 (2003) R1257–R1289.
[31] F. Xu, Z. Li, L. Wu, Q. Meng, H. Xin, J. Sun, B. Ge, L. Sun, Y. Zhu, Nanomater. Energy 30 (2016) 771–779.
[32] P. Gao, Y.Y. Zhang, L. Wang, S. Chen, Y. Huang, X. Ma, K. Liu, D. Yu, Nanomater. Energy 32 (2017) 302–309.
[33] X. Liu, K. Zhang, K. Lei, F. Li, Z. Tao, J. Chen, Nano Res 9 (2016) 198–206.
[34] J. Li, Y. Fu, X. Shi, Z. Xu, Z. Zhang, Chem. Eur J. 23 (2017) 157–166.
[35] D. Chao, P. Liang, Z. Chen, L. Bai, H. Shen, X. Liu, X. Xia, Y. Zhao, S.V. Savilov, J. Lin, Z.X. Shen, ACS Nano 10 (2016) 10211–10219.
[36] Z. Shadike, Y.N. Zhou, F. Ding, L. Sang, K.W. Nam, X.Q. Yang, Z.W. Fu, J. Power Sources 260 (2014) 72–76.
[37] K. Chen, K. Cao, C. Xing, Y. Hu, J. Liu, Y. He, J. Wang, A. Li, H. Qin, J. Alloy. Comp. 688 (2016) 946–952.
[38] Q. Su, S. Wang, Y. Xiao, L. Yao, G. Du, H. Ye, Y. Fang, J. Phys. Chem. C 121 (2017) 3295–3303.
[39] J. Li, M. Zou, L. Chen, Z. Huang, L. Guan, J. Mater. Chem. A 2 (2014) 10634–10638.
[40] Q. Su, D. Xie, J. Zhang, G. Du, B. Xu, ACS Nano 7 (2013) 9115–9121.
[41] Q. Su, G. Du, J. Zhang, Y. Zhong, B. Xu, Y. Yang, S. Neupane, K. Kadel, W. Li, ACS Nano 7 (2013) 11379–11387.
[42] M.B. Pinson, M.Z. Bazant, J. Electrochem. Soc. 160 (2013) A243–A250.
[43] P. Ge, H. Hou, X. Ji, Z. Huang, S. Li, L. Huang, Mater. Chem. Phys. 203 (2018) 185–192.
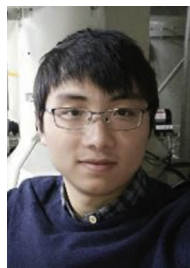
Libing Yao is currently pursuing his Ph.D. degree at Key Laboratory of MEMS of the Ministry of Education, Southeast University, Nanjing. He received his Master's degree in Physical Chemistry from Zhejiang Normal University in 2017. His research interests involve the design and synthesis of novel functional materials for energy storage and *in situ* TEM study of lithium/sodium-ion batteries.

Weiwei Xia is currently pursuing her Ph.D. degree in Key Laboratory of MEMS of the Ministry of Education in Southeast University, Nanjing. She received her Bachelor's degree and Master's degree in Physical Electronics from Zhengzhou University in 2010 and 2014, respectively. Her research interests involve the design and synthesis of novel nanostructured materials for energy storage and *in situ* transmission electron microscopy.
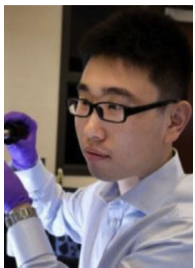
Hongtao Zhang received his Bachelor's degree from Southeast University in 2014. He is now continuing his studies as a Ph.D. candidate at Key laboratory of MEMS of Ministry of Education, Southeast University. His research interests include the synthesis and the *in situ* TEM study of novel nanomaterials.

Dr Hui Dong is currently working at Key Laboratory of Welding Robot and Application Technology of Hunan Province, Xiangtan University, Hunan province, China. He obtained his Ph.D. in 2018 from Southeast University. He was a Visiting Scholar at the Queensland University of Technology from 2016 to 2017. Currently, he concentrates on *in situ* Transmission and Scanning electron microscopy study on morphology and structure property relationship of nanomaterials, under multi field coupling including force, heat, optical, electric fields and so on.

Yi Wu is currently pursuing her Ph.D. degree in Key Laboratory of MEMS of the Ministry of Education in Southeast University, Nanjing, China. She received her Bachelor's degree in Physical Electronics from Anhui University in 2016. Her research interests focus on the synthesis of novel 1D nanomaterials and related energy storage.

Dr. Huolin L. Xin is now an Associate Professor Department of Physics and Astronomy, University of California, Irvine, California, U.S.A. He received his Bachelor's degree from Peking University in 2005 and Ph.D. from Cornell University in 2011, respectively. He was a post-doctoral fellow in Lawrence Berkeley National Laboratory (2011–2013) and a staff material scientist in Brookhaven National Laboratory (2013–2018). He is interested in developing novel 3-D, atomic-resolution, *in situ* spectroscopic and imaging tools to probe the structural, chemical, and bonding changes of energy materials.

Dr. Meng Nie is an Associate Professor in the Key Laboratory of MEMS of the Ministry of Education at Southeast University (SEU), Nanjing, China. She obtained her Ph.D. in 2007 from Southeast University and was promoted to an Associate Professor in 2011, respectively. She was a post-doctor in Delft University of Technology from 2011 to 2012. Currently, her research interests include MEMS/NEMS devices such as pressure sensors.

Dr. Peng Gao is currently a Professor in School of Physics, Peking University, Beijing, China. He received his Ph.D. degree in 2010 from the Institute of Physics, Chinese Academy of Sciences. He was a post-doctoral fellow in University of Michigan (2010–2013), a research associate in Brookhaven National Laboratory (2013–2014), and a research fellow in in University of Tokyo (2014–2015). He was selected in Project of Thousand Youth Talents and then joined in Peking University in 2015. His research interests include electron microscopy, ferroelectrics, solid-state ionics, and structure and properties of crystal defects and interfaces.
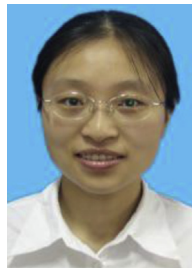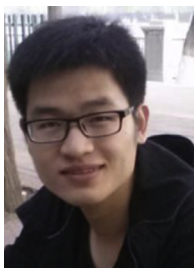
Dr. Shuangying Lei is an Associate Professor in the Key Laboratory of MEMS of the Ministry of Education at Southeast University (SEU), Nanjing, China. She obtained her Ph.D. in 2006 from Peking University and was promoted to an Associate Professor in 2009, respectively. She was a Visiting Scholar in Rensselaer Polytechnic Institute from 2014 to 2015. Currently, she mainly employs density functional theory calculations to study structure-property relationship of nanomaterials.

Ran Cai is now a Ph.D. candidate at Key laboratory of MEMS of Ministry of Education, Southeast University, Nanjing, China. She received her Bachelor's degree and Master's degree from Nanjing University of Posts and Telecommunications in 2013 and 2016, respectively. Her research interests focus on the *in situ* TEM observation of electrochemical behaviors of nanomaterials.

Dr. Litao Sun is currently a Distinguished Professor at Southeast University, Nanjing, China. He received his Ph.D. from the Shanghai Institute of Applied Physics, Chinese Academy of Sciences, followed by postdoctoral research at University of Mainz, Germany and a visiting professorship at the University of Strasbourg, France. His current research interests include *in situ* experimentation inside the electron microscope, graphene and related 2D materials, new phenomena from sub-10 nm nanoparticles, and applications of nanomaterials in environment, energy, and nanoelectromechanical systems.

Chongyang Zhu is now studying as a Ph.D. candidate at Key laboratory of MEMS of Ministry of Education, Southeast University, Nanjing, China. He received his Bachelor's degree from Nanjing University of Posts and Telecommunications in 2013. His research interests include the synthesis and applications of novel nanomaterials for energy storage and conversion systems, as well as *in situ* TEM study of lithium/sodium-ion batteries.

Dr. Feng Xu is a Professor in the Key Laboratory of MEMS of the Ministry of Education, Southeast University (SEU), Nanjing, China. He obtained his Ph.D. in 2009 from Nanjing Tech University. In 2012 and 2017, he was promoted to Associate Professor and Professor, respectively. He was a Visiting Scholar at Brookhaven National Laboratory from 2014 to 2015. Currently, he concentrates on study of structure-property relationship of nanomaterials, including but not limited to energy conversion and storage materials, by using *in situ* transmission electron microscopy.